Contactless Visualization of Fast Charge Carrier Diffusion in Hybrid Halide Perovskite Thin Films

Kathrin Handloser, Nadja Giesbrecht, Thomas Bein, Pablo Docampo,* Matthias Handloser,* and Achim Hartschuh*

Department of Chemistry and Center for NanoScience (CeNS), Ludwig-Maximilians-Universität München, Butenandtstr. 5-13, 81377 Munich, Germany

Nanosystems Initiative Munich (NIM), Ludwig-Maximilians-Universität München, Schellingstr. 4, 80799 Munich, Germany

S *Supporting Information*

ABSTRACT: Organic−inorganic metal halide perovskite solar cells have recently attracted considerable attention with reported device efficiencies approaching those achieved in polycrystalline silicon. Key for an efficient extraction of photogenerated carriers is the combination of low nonradiative relaxation rates leading to long carrier lifetimes and rapid diffusive transport. The latter, however, is difficult to assess directly with reported values varying widely. Here, we present an experimental approach for a contactless visualization of the charge carrier diffusion length and velocity in thin films based on time-resolved confocal detection of photoluminescence at varying distances from the excitation position. Our measurements on chloride-treated methylammonium lead iodide thin films, the material for which the highest solar cell efficiencies have been reported, reveal a charge carrier diffusion length of 5.5−7.7 μm and a transport time of 100 ps for the first micrometer corresponding to a diffusion constant of about 5−10 cm^2 s^{-1}, similar to GaAs thin films.

KEYWORDS: *perovskites, solar cells, thin films, hybrid materials, photoluminescence, charge transport*
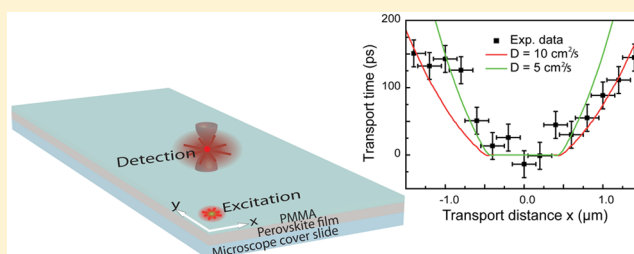
The field of organic−inorganic lead halide perovskite absorbers and their application in solar cells has seen an unprecedented development during the past 4 years with extremely fast progress taking efficiencies from 10% in 2012[1] to over 19% in 2015.[2,3] This family of materials has the potential to fulfill most requirements for large scale production as the fabrication is compatible with solution-processing techniques, the materials are cheap and readily available and high efficiencies, comparable to those of thin film solar cells incorporating poly crystalline silicon[4] or copper indium gallium selenide (CIGS),[5] have already been achieved.

While perovskite absorber layers were initially employed to replace the dye in mesoporous TiO$_2$ sensitized solar cells,[6] the system was later extended to function efficiently on electronically inactive scaffolds and finally in a planar configuration.[1,7−9] This final structure is the current state-of-the-art device architecture performing at a reported power conversion efficiency of 19.3%.[10] The photophysical properties of hybrid halide perovskite thin films have recently been investigated by a number of groups.[11−16] Upon optical excitation weakly bound excitons are created that are expected to rapidly dissociate into free charge carriers at room temperature.[11]

To determine the charge carrier diffusion length in thin films, a straightforward approach is the fabrication of a series of contacted devices with increasing active layer thickness while recording the decrease in photocurrent. Using this procedure, a minimum diffusion length of 400 nm was found for one-step

solution processed films,[8] and about 1 μm for dual source vacuum deposited films.[17] Previously, diffusion lengths have also been extracted from photoluminescence (PL) measurements,[7,18−20] impedance spectroscopy,[21] intensity modulated spectroscopy,[22] terahertz spectroscopy,[23,24] microwave conductivity,[25] and electron beam-induced current measurements.[26,27] Additionally, two techniques based on a spatio-temporal detection scheme allowing for the real-time tracking of the kinetics of photoexcited minority carriers have recently been introduced using time-resolved photoluminescence and transient absorption microscopy.[28,29] Depending on the investigated material and the applied experimental technique, the resulting diffusion lengths range between 100 nm and 6.3 μm corresponding to diffusion constants for thin films between 0.02 cm^2 s^{-1} and several cm^2 s^{-1}.[19,30] To avoid both spatial averaging and the influence of different contact materials, a contactless, noninvasive microscopic optical method to visualize the charge carrier transport properties in perovskite thin films is needed.

The photovoltaic performance of perovskite-based photovoltaic devices was recently found to depend on certain preconditioning steps.[31−34] Among these, extended illumination with light was observed to drastically increase the power
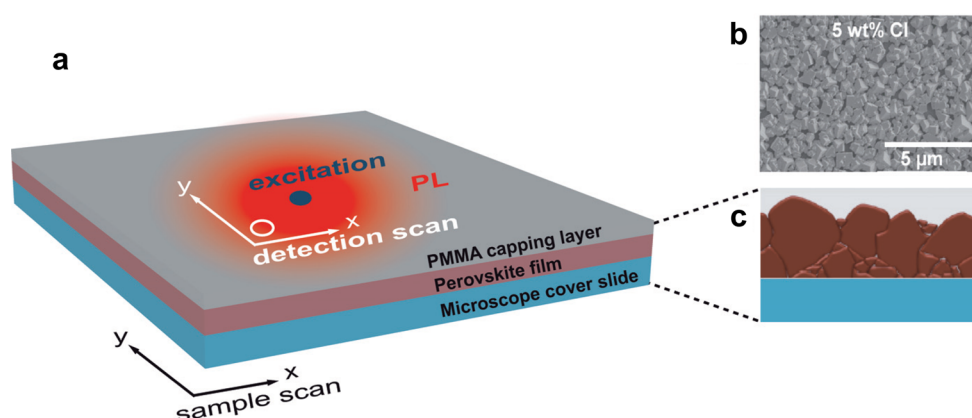
Figure 1. Schematic illustration of the experimental approach and the sample layout. (a) Two different confocal scanning modes are implemented: In sample scans, both excitation and detection remain fixed, while the PL is recorded as a function of sample position. In detection scans, the excitation and sample position are fixed while the detection is scanned. Photoluminescence (red area) observed at remote detection areas clearly indicates energy transport within the film. The investigated halide perovskite film is spin-coated onto a standard microscope cover slide and top coated by a thin PMMA layer to prevent the material from degradation effects. (b) Scanning electron micrograph showing a top view of the investigated chloride-treated perovskite film with connected crystallites of varying size and orientation. Scale bar: 5 μm. (c) Schematic cross-section displaying the typical morphology of the deposited perovskite film with a nonuniform crystal size distribution.[39] With the applied measurement configuration, we expect to mainly probe the quasi-continuous film at the bottom.
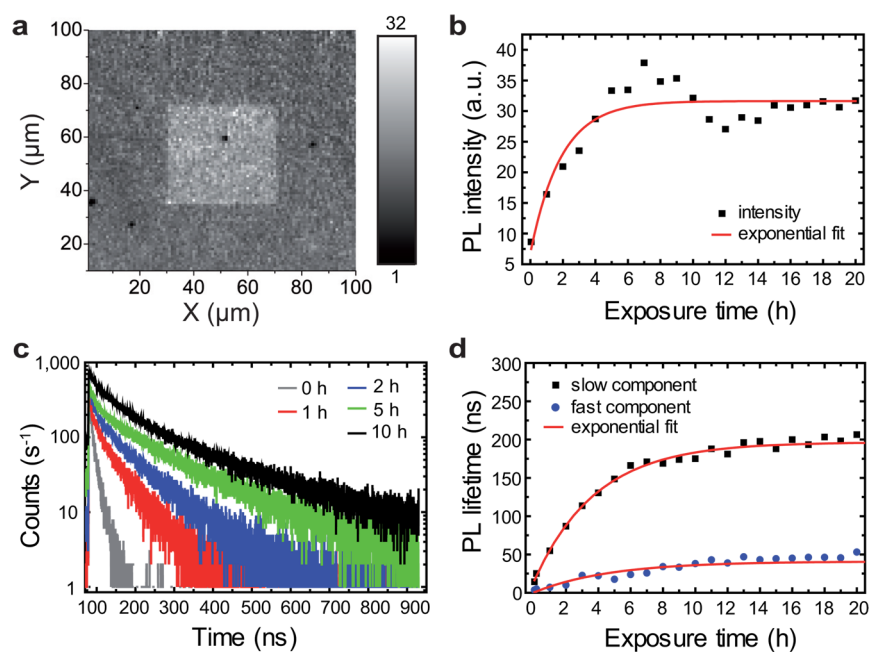

Figure 2. Evolution of light soaking with increasing exposure time to light. (a) Photoluminescence map of a 100 × 100 μm^2 large area within the investigated perovskite thin film obtained by raster-scanning the sample at a low excitation power of 10 nW. The bright central square has been presoaked by raster-scanning the respective area at high pump-fluence ($P \sim 500$ nW) for 150 ms per pixel. (b) PL intensity recorded as a function of exposure time at a pump-fluence of 10 nW. With increasing exposure time to light, the PL intensity significantly increases before reaching saturation after ~10 h. (c) Corresponding time-resolved PL transients. The decay slows down with increasing exposure time and reaches a stable value after ~10 h. (d) Fast and slow component of the PL decay extracted from biexponential fitting of the PL transients shown in (c). Both contributions can be modeled by a single exponential rise function indicating that the microscopic process leading to light soaking follows first order reaction kinetics involving a single rate-determining step.

conversion efficiency and thus is a prerequisite for the optimum operation of most of the devices presented in the literature.[8,35−37] However, the microscopic origin of this so-called light soaking effect so far remains unclear. Yet, to investigate and discuss the transport of photogenerated species in lead halide perovskite thin films, the quantification of the influence of light soaking on the optical properties is clearly essential to guarantee stable and reproducible measurement conditions.

In the present work, we first study the effect of light soaking on the photoluminescence properties of chloride-treated methylammonium lead iodide (MAPI) perovskite thin films. Upon light exposure, the PL intensity of the illuminated sample volume increases about 5-fold due to decreasing nonradiative relaxation rates as observed in simultaneously recorded PL transients. The photoinduced process observed during light soaking follows first order kinetics indicating a single rate-determining step leading to a stable final state. Remarkably,

excited charge carriers generated in the film by focused excitation lead to light soaking up to several micrometers in the surrounding sample volume indicating long-ranged diffusion. Contactless measurements of the diffusion length and transport time of charge carriers in fully soaked sample volumes are subsequently performed by time-resolved laser scanning confocal PL microscopy in which the detection volume is raster-scanned with respect to the fixed excitation volume. PL transients detected for increasing distances show a delayed rise while a transport time of 100 ps is observed for the first micrometer. Simple numerical simulations of the diffusion process considering the measured PL lifetimes reproduce the observed delay for a diffusion constant of $D \sim 5-10$ cm^2 s^{-1}. The diffusion length $L_D = \sqrt{D \cdot \tau} \sim 5.5-7.7$ μm, calculated from the measured charge carrier lifetime τ, considerably exceeds the average single grain size of $\sim$200 nm observed in scanning electron micrographs, while the observed transport speed is comparable to that of GaAs thin films at room temperature.[38]

■ RESULTS AND DISCUSSION

Figure 1 schematically illustrates the applied experimental approach as well as the sample architecture. The experimental setup enables two different confocal scanning modes, either a sample scan or a detection scan (Figure 1a). With these experimental techniques, we detect the PL signal arising from the recombination of photoexcited states as a measure for the carrier density within the film.

Chloride-treated methylammonium lead iodide thin films are fabricated via a two-step deposition protocol using PbI$_2$ films and methylammonium iodide and chloride solutions.[1,7] The investigated perovskite film is deposited onto a standard microscope cover slide and subsequently coated by a thin PMMA layer to protect the material from degradation effects. A top view of the film is displayed in the scanning electron micrograph in Figure 1b showing connected crystallites of varying size and orientation. The average film thickness was estimated from SEM cross sections to be $\sim$325 nm and the average crystal size $\sim$230 nm (see Supporting Information, Figure S1). In Figure 1c, the typical morphology of the investigated film is illustrated as a schematic cross section. Recent studies on the crystallization process of perovskite films deposited via the employed two-step technique showed a nonuniform distribution of crystal sizes within the fabricated films.[39] Whereas small crystallites form the bottom layer of the perovskite film, larger crystals can be found on top due to Ostwald-type ripening at the surface. The studied films have an optical density of OD = 1.1 at the excitation wavelength of 510 nm and an average thickness of around 325 nm. The $1/e$ length of the excitation intensity is thus around 120 nm, and we expect to mainly probe the lower third of the film.

An examination of the light soaking effect mentioned above and of its impact on the optical properties of the studied films is a prerequisite for any transport measurement aiming to quantify the diffusion length and speed. Figure 2a shows the photoluminescence map of the investigated perovskite film at low excitation power $P \sim 10$ nW corresponding to a power density of $\sim$14.15 W cm^{-2}, which is about 20× the intensity of 1.5 AM equivalent sunlight illumination. Included in the PL map is a smaller scan area (40×40 μm^2) that was previously exposed to light by raster-scanning at higher pump-fluence ($P \sim 500$ nW; power density ~ 707 W cm^{-2}). The PL intensity significantly increased in the presoaked area as can be seen

from the brighter, central square in the PL map. We observe the PL intensity (Figure 2b) to increase by a factor of $\sim$5 with increasing exposure time to light, saturating after $\sim$10 h. At the same time, the shape and position of the PL spectra remain unchanged (see Supporting Information, Figure S2) indicating that light soaking has no influence on the energy of the emitting state. Remarkably, the μm transport range observed in Figures 3 and 4 below clearly exceeds the average crystallite size seen in
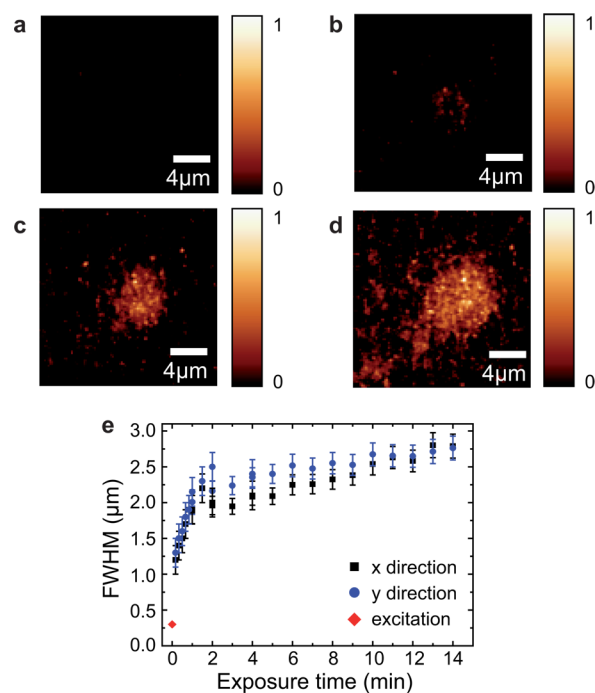

Figure 3. Visualization of charge transport via light soaking. (a−d) Series of PL sample scans of the same film area recorded at low excitation power ($\sim$10 nW) after focused excitation at the center at higher power ($\sim$4 μW) for (a) $t = 0$ s, (b) 60 s, (c) 300 s, and (d) 840 s with identical intensity scaling. Increasing exposure time leads to intensive brightening of the PL signal and to a significantly larger area of emission indicating that photoexcited carriers lead to light soaking in sample regions that are not illuminated directly. At the same time, nonradiative loss channels are reduced, which leads to the observed higher PL intensity and extended charge carrier lifetimes. Scale bar of all PL maps: 4 μm. (e) Fwhm obtained from 2D Gaussian fits of the recorded PL maps. The corresponding fwhm increase with exposure time to light and are significantly larger than the width of the diffraction-limited excitation spot of 300 nm. Displayed error bars reflect the standard deviation of the Gaussian fits.

the SEM micrograph in Figure 1b. We thus attribute this to efficient diffusive charge carrier transport through the continuous underlayer depicted in Figure 1c and demonstrated in a previous publication[7] that is not apparent in the topview SEM micrograph. For the pump-fluences applied here, light soaking of the investigated sample material is found to be an irreversible process that reaches a stable final state. In contrast, for mixed iodide and bromide-based perovskite films reversible soaking has been reported at very low excitation fluences of $\sim$15 mW cm^{-2}.[40]

To gain insight into the dynamics of this light soaking process, the evolution of light soaking with exposure time to light was studied via time-correlated single photon counting (TCSPC). The corresponding transients are shown in Figure 2c and can be described by a biexponential decay
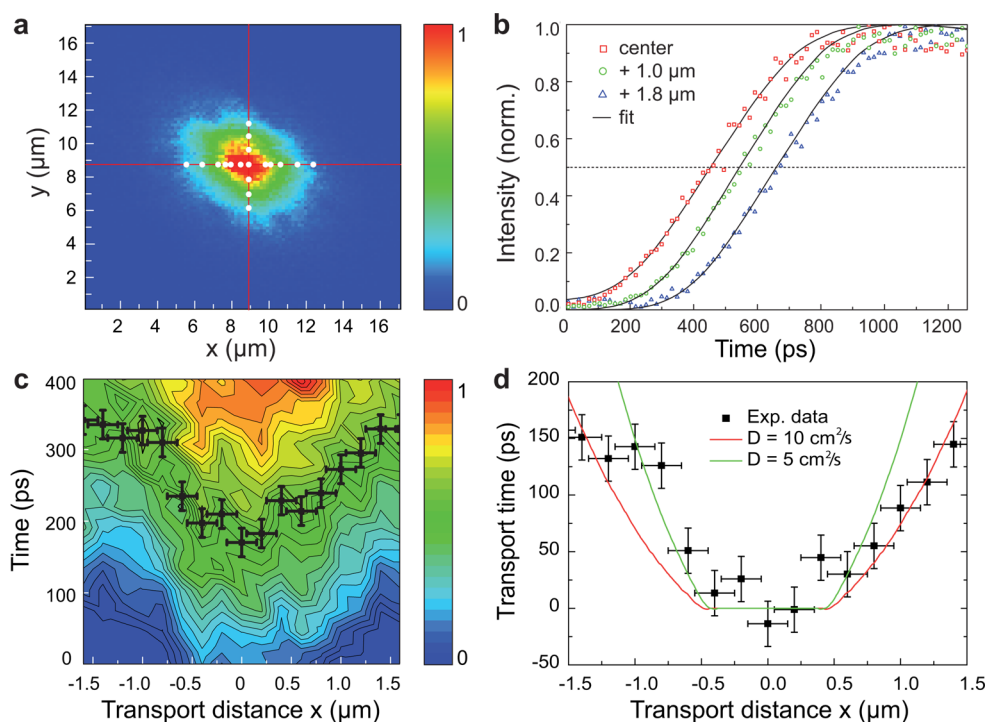
Figure 4. Spatial and temporal investigation of diffusive transport after the elimination of light soaking effects. (a) Detection beam scan of the steady-state PL signal for a fixed excitation position using uniformly light soaked material. Diffusive transport is spatially visualized within a range of 3 μm, since emission can be detected up to 3 μm apart from the excitation spot. (b) Zoom-in to the rise of the PL transients recorded upon femtosecond pulsed excitation at 730 nm at increasing excitation-detection distances (white dots in (a)). (c) False color plot of the normalized TCSPC transients recorded for increasing excitation-detection distances in $\pm x$ direction. The black crosses mark the times at which the PL intensity reaches 50% of its maximum taken as the transport times shown in (d). (d) Transport times for diffusive carrier transport in $\pm x$ direction. Transport times are extracted from recorded TCSPC transients to be within a range of 100 ps for the first micrometer. Displayed y-error bars represent the error obtained from the fitting routine, while the x-error bars represent the uncertainty created by the finite excitation size of ± 150 nm. The solid lines are simulations of diffusive transport using the 2D diffusion equation and different diffusion constants. The measured data indicate a diffusion constant of about $D \sim 5-10$ cm^2 s^{-1} for the investigated perovskite thin film, which is comparable to the value of GaAs thin films at room temperature.[38]

function,[7,20,41] indicating two different types of emissive states that contribute to the PL decay. With continuous illumination, the PL decay slows down and reaches a stable value after about 10 h at the used power density. Biexponential modeling of the decay dynamics allows for the extraction of the fast and the slow PL lifetime (Figure 2d), which both increase with increasing exposure time. Since the PL intensity increases along with the lifetime we attribute light soaking to the lowering of the nonradiative decay rate caused by the filling of trap states or other quenching sites. The dependence of both lifetimes on the exposure time t_{exp} can be properly modeled by a single exponential rise function $\propto (1 - \exp(-k_{soaking} t_{exp}))$ with comparable rate constants $k_{soaking}$ of 0.21 and 0.26 h^{-1} for the used excitation intensity. The monoexponential rise of the two lifetimes seen in Figure 2d indicates that the microscopic process leading to light soaking follows first order reaction kinetics involving a single rate-determining step.

Since light soaking is a dynamic effect with nonstationary sample properties, we can either study fully soaked or completely unsoaked material. Whereas the first option allows for the investigation of a stable system, the latter can even enable the monitoring of transport within the film provided that the transported species lead to the same effect that causes light soaking as direct laser excitation. In Figure 3a−d, a consecutive series of PL sample scans of the same sample area is shown. Starting from entirely unsoaked material (Figure 3a), the fixed center of the scanned area was illuminated with high excitation power ($P \sim 4$ μW; power density = 1.4 kW cm^{-2}) for

six intervals of 10 s, followed by longer intervals of 60 s up to a total of 14 min between consecutive scans. PL sample scans were then recorded at low intensity ($P \sim 10$ nW) to reduce soaking effects resulting from image acquisition to a minimum. With continuous photoexcitation at the center of the scanned area, a significantly increased emission area as well as an intensive brightening of the PL spot can be observed (Figure 3a−d). Because light soaking of the investigated sample material was found to be an irreversible process for the applied pump-fluences, the time between a soaking interval and the subsequent PL measurement is not essential for the reported observation. To minimize the experimental error due to focal drift, every soaking interval was immediately followed by the subsequent PL scan and vice versa, with the result that only a few seconds passed in between each of the two steps.

The recorded PL maps were modeled with 2D Gaussian fits to evaluate the size of the photoluminescent area for each illumination step. The full width at half-maximum (fwhm) obtained from the individual fits are shown in Figure 3e with the corresponding exposure time to light. We find the fwhm to grow with increasing exposure time and being of similar extension in the x and y directions. Slight deviations can be attributed to film inhomogeneities. With respect to the diffraction-limited excitation spot featuring a width of 300 nm, the fwhm of the resulting PL area is significantly larger and light soaking effects can still be observed several microns away from excitation. These findings give evidence that transport within the investigated film occurs on the length scale of several

microns. Furthermore, they demonstrate that photoexcited carriers lead to light soaking in sample regions that are not directly exposed to light. The contribution of elastic scattering of the excitation light to the emergence of light soaking effects in remote areas can be excluded since the same experimental results have been obtained via two-photon excitation, which provides efficient background suppression (see Supporting Information, Figure S3).

For the excitation fluences used in the experiments light absorption is expected to lead to moderate sample heating in the range of 10 K directly in the focus (see Supporting Information). The temperature increase several microns away from the photoexcited volume can probably be neglected. Thermally activated annealing of the film is thus unlikely to be responsible for the observed light soaking effect in the present case.

Next, we investigated the spatial range of carrier transport within the film and the time-scale of the diffusion process on fully soaked material that has reached a steady-state after extended light exposure (Figure 2). We can thus exclude any influence of light soaking on the extracted transport characteristics. Figure 4a shows a detection beam scan of the steady-state PL signal for a fixed excitation position. PL is detected up to a distance of more than 3 μm, substantially exceeding the width of the excitation spot of 300 nm. This observation forms the basis for our approach to determine the transport times of charge carriers and the diffusion constant.

In the key experiment, PL transients are detected at increasing distances between detection and excitation volume. The acquired PL transients (Figure 4b,c) show a continuously growing shift in the signal rise for increasing excitation-detection distances which enables the observation of transport as a function of time. The PL transients recorded for different excitation-detection distances are referenced to the PL transient at the center position (red curve in Figure 4b). This allows for the extraction of the charge carrier transport times as a function of distance (black squares in Figure 4d) that we identify here as the time at which the PL intensity at a given distance reaches 50% of its maximum value. Our experimental findings reveal a transport range of more than 3 μm as visible from the PL map in Figure 4a and a transport time of ~100 ps for the first micrometer (Figure 4d).

Numerical simulation results using the 2D diffusion equation and considering the measured intensity-averaged lifetime τ are shown in Figure 4d (solid lines) for different diffusion constants D (see Supporting Information). Within our measurement accuracy of about 20 ps (Supporting Information, Figure S5), the experimental values match the simulated data reflecting a diffusion constant of $D \sim 5-10$ cm^2 s^{-1}, which is comparable to the value of GaAs thin films at room temperature.[38] Due to the spatial heterogeneity of the perovskite film, the diffusion constant D is expected to vary for different film positions, while the values noted above are found to be typical. The diameter of both excitation and detection focus of around 300 nm will lead to spatial broadening of the observed PL distribution. To determine the influence of this broadening on the derived transport times we included the finite focal size in our simulations (Supporting Information, Figure S6). Considering the parameters of the microscope system we find that this mainly affects the apparent transport times within the width of the excitation focus while the influence on the derived transport times for increasing transport distances remains small compared to the experimental

noise (Figure 4d). To complement our analysis based on the transport time we also studied the transport by plotting the spatial PL intensity profiles at increasing time-delay after pulsed excitation following the procedure described in ref 29. The resulting profiles for the derived diffusion constant are in reasonable agreement with numerical simulations based on the 2D diffusion model supporting our approach (Supporting Information, Figure S7).

Using the derived diffusion constant D and the measured intensity-averaged PL lifetime of about 60 ns, we calculate the diffusion length as $L_D = \sqrt{D \cdot \tau} = 5.5-7.7$ μm. The somewhat larger diffusion length observed here, as compared to the existing literature,[19,20,25] could result from the contactless probing enabled by the presented technique, which gives access to the intrinsic transport properties excluding possible perturbations from electrodes or additional surface layers and the clear distinction of the effect of light soaking. The present values for the diffusion constant and length observed for chloride-derived MAPI films are distinctly different from those reported by Guo et al. in ref 29 for flakes synthesized from a one-step stoichiometric precursor mixture of MAPI using transient absorption microscopy.

We note that the results shown in Figure 4 and the extracted transport characteristics have been obtained for fully light-soaked films. Because of the light soaking effect at the excitation position and its increasing range (Figure 3), no reliable and meaningful results can be obtained for unsoaked or intermediately soaked films. For unsoaked films the diffusion length is expected to be significantly shorter due to the measured shorter intensity averaged PL lifetime, which is reduced from 60 to 6 ns (Figure 2d and Supporting Information, Figure S4). This is also in agreement with the smaller width of the area of increased PL intensity for short exposure times observed in Figure 2. As discussed above, the large transport length greatly exceeding the crystallite size observed in the SEM micrograph (Figure 1b) is attributed to efficient diffusive charge carrier transport through the continuous underlayer (Figure 1c).

The observed transport time of ~100 ps for the first micrometer shows that diffusive transport occurs on a much faster time-scale than PL decay with lifetimes reaching beyond 100 ns. The observation of biexponential PL decay for localized detection, however, needs further discussion. If the radiative relaxation of the mobile species would be the origin of the detected PL, diffusive transport would lead to a very fast nonexponential decay following $\propto 1/t$ at the excitation focus. The observed PL with biexponential decay thus needs to result from a nonmobile state that is rapidly populated by the mobile species during diffusive transport. We speculate that in the studied film PL emission results from nonmobile excitons that could be localized by shallow energy traps or by self-trapping.

■ CONCLUSIONS

The results presented above illustrate that highly efficient diffusive charge transport can be achieved in solution processed nanocrystalline thin films of chloride-treated methylammonium lead iodide. The observed diffusion length of several micrometers can be attributed to a high charge carrier mobility, which is comparable to that of GaAs thin films, and long carrier lifetimes reaching into the 100 ns range. Here, light soaking is seen to play an important role for reducing nonradiative losses in as-prepared films. The described method for the contactless

characterization of transport properties allows for the rapid screening of differently prepared films without the need of electrical contacting and has the potential to become an important and routine tool for the characterization of hybrid halide perovskite thin films.

METHODS

Perovskite Film Preparation. Methylammonium iodide and chloride were prepared following a previously published protocol.[1,7] In short, 24 mL of methylamine solution (33% in ethanol) were diluted using 100 mL of absolute ethanol. Under constant stirring, 10 mL of an aqueous hydriodic acid solution (57 wt %) or 15 mL of concentrated hydrochloric acid (37% in water) were added to this solution. After having reacted for 1 h at room temperature, the solvents were removed by rotary evaporation. The obtained white solid was washed with dry diethyl ether and recrystallized from ethanol. Lead iodide (99% Sigma) and anhydrous N,N-dimethylformamide (DMF, Sigma) were used as received. A ~200 nm thick layer of lead iodide was deposited via dynamic spin-coating from a 0.85 M PbI$_2$ solution in DMF at 3000 rpm for 15 s on a standard 160 μm thick glass cover slide. When starting the spin-coater, a temperature between 60 and 65 °C is required for both the substrate and the precursor solution[7] to achieve visually smooth films. The immersion solutions were prepared by dissolving 9.5 mg mL^{-1} methylammonium iodide and 0.5 mg mL^{-1} methylammonium chloride in anhydrous isopropanol (Sigma) through heating to 60 °C. The spin-coated films were then immersed in the heated solutions for 8 min, while the temperature of the solution was monitored and kept at 60 ± 1 °C for the entire time. Once the conversion was finished, the perovskite films were washed with clean, anhydrous isopropanol and dried under a nitrogen stream. The final perovskite film featured an average thickness of 325 nm, which was estimated via scanning electron microscopy cross sections. After synthesis, the films were covered with a poly(methyl methacrylate) (PMMA) layer to protect the films from degradation through moisture. For this purpose, 50 mg mL^{-1} of PMMA in anhydrous chlorobenzene was spin-coated at 1000 rpm.

Laser Scanning Confocal Microscopy. The experimental setup is based on a confocal optical microscope equipped with a closed-loop piezo scan stage (sample scan) to raster-scan the sample through the focus of a high NA objective (NA = 1.4). Laser excitation is provided by a pulsed diode operating at 510 nm and a repetition rate of 1 MHz. For the transport studies in the sub-ns regime a faster Ti:sapphire laser was used providing ~200 fs pulses at 730 nm at a rate of 3.8 MHz. The detection beam path is equipped with a closed-loop piezo scan mirror (detection scan) and an avalanche photodiode (APD) in combination with electronics for time-correlated single photon counting (TCSPC). The resulting instrument response function has a temporal width of 38 and 440 ps in the case of the Ti:sapphire laser and the pulsed diode, respectively (Supporting Information, Figure S5). The focal length of the collimation optics was chosen to form a diffraction limited detection spot with a diameter of ~300 nm that can be raster-scanned with respect to the fixed excitation position (Supporting Information). For the light soaking experiments in Figure 3, a laser excitation power of ~4 μW was applied corresponding to a power density of 1.4 kW cm^{-2}. Confocal PL images were recorded using a lower excitation power of ~10 nW.

ASSOCIATED CONTENT

Ⓢ Supporting Information

The Supporting Information is available free of charge on the ACS Publications website at DOI: 10.1021/acsphotonics.5b00562.

Crystal size distribution of investigated film, PL spectra during light soaking, charge transport via light soaking upon two-photon excitation, intensity fractions of fast and slow component during light soaking and estimation of sample heating. Numerical modeling of the diffusion data and influence of the diameter of excitation and detection focus on the derived transport properties. Dynamics of the spatial PL intensity profiles after pulsed excitation (PDF).

AUTHOR INFORMATION

Corresponding Authors
*E-mail: pablo.docampo@cup.lmu.de.
*E-mail: matthias.handloser@cup.lmu.de.
*E-mail: achim.hartschuh@cup.lmu.de.
Notes
The authors declare no competing financial interest.

ACKNOWLEDGMENTS

REFERENCES

(1) Lee, M. M.; Teuscher, J.; Miyasaka, T.; Murakami, T. N.; Snaith, H. J. Efficient Hybrid Solar Cells Based on Meso-Superstructured Organometal Halide Perovskites. *Science* **2012**, *338*, 643−647.
(2) Green, M. A.; Ho-Baillie, A.; Snaith, H. J. The Emergence of Perovskite Solar Cells. *Nat. Photonics* **2014**, *8*, 506−514.
(3) Green, M. A.; Bein, T. Perovskite Cells Charge Forward. *Nat. Mater.* **2015**, *14*, 559−561.
(4) Saga, T. Advances in Crystalline Silicon Solar Cell Technology for Industrial Mass Production. *NPG Asia Mater.* **2010**, *2*, 96−102.
(5) Jackson, P.; Hariskos, D.; Wuerz, R.; Kiowski, O.; Bauer, A.; Magorian Friedlmeier, T.; Powalla, M. Properties of Cu(In,Ga)Se$_2$ Solar Cells with New Record Efficiencies Up To 21.7%. *Phys. Status Solidi RRL* **2015**, *9*, 28−31.
(6) Kojima, A.; Teshima, K.; Shirai, Y.; Miyasaka, T. Organometal Halide Perovskites As Visible-Light Sensitizers for Photovoltaic Cells. *J. Am. Chem. Soc.* **2009**, *131*, 6050−6051.
(7) Docampo, P.; Hanusch, F.; Stranks, S. D.; Döblinger, M.; Feckl, J. M.; Ehrensperger, M.; Minar, N. K.; Johnston, M. B.; Snaith, H. J.; Bein, T. Solution Deposition-Conversion for Planar Heterojunction Mixed Halide Perovskite Solar Cells. *Adv. Energy Mater.* **2014**, *4*, 1400355.
(8) Docampo, P.; Ball, J. M.; Darwich, M.; Eperon, G. E.; Snaith, H. J. Efficient Organometal Trihalide Perovskite Planar-Heterojunction Solar Cells on Flexible Polymer Substrates. *Nat. Commun.* **2013**, *4*, 2761.
(9) Eperon, G. E.; Burlakov, V. M.; Docampo, P.; Goriely, A.; Snaith, H. J. Morphological Control for High Performance, Solution-Processed Planar Heterojunction Perovskite Solar Cells. *Adv. Funct. Mater.* **2014**, *24*, 151−157.

(10) Zhou, H.; Chen, Q.; Li, G.; Luo, S.; Song, T.-B.; Duan, H.-S.; Hong, Z.; You, J.; Liu, Y.; Yang, Y. Interface Engineering of Highly Efficient Perovskite Solar Cells. *Science* **2014**, *345*, 542−546.

(11) D'Innocenzo, V.; Grancini, G.; Alcocer, M. J. P.; Ram Srimath Kandada, A.; Stranks, S. D.; Lee, M. M.; Lanzani, G.; Snaith, H. J.; Petrozza, A. Excitons Versus Free Charges in Organo-Lead Tri-Halide Perovskites. *Nat. Commun.* **2014**, *5*, 3586.

(12) Zhu, H.; Fu, Y.; Meng, F.; Wu, X.; Gong, Z.; Ding, Q.; Gustafsson, M. V.; Trinh, M. T.; Jin, S.; Zhu, X.-Y. Lead Halide Perovskite Nanowire Lasers with Low Lasing Thresholds and High Quality Factors. *Nat. Mater.* **2015**, *14*, 636−642.

(13) Deschler, F.; Price, M.; Pathak, S.; Klintberg, L. E.; Jarausch, D.-D.; Higler, R.; Hüttner, S.; Leijtens, T.; Stranks, S. D.; Snaith, H. J.; et al. High Photoluminescence Efficiency and Optically Pumped Lasing in Solution-Processed Mixed Halide Perovskite Semiconductors. *J. Phys. Chem. Lett.* **2014**, *5*, 1421−1426.

(14) Tvingstedt, K.; Malinkiewicz, O.; Baumann, A.; Deibel, C.; Snaith, H. J.; Dyakonov, V.; Bolink, H. J. Radiative Efficiency of Lead Iodide Based Perovskite Solar Cells. *Sci. Rep.* **2014**, *4*, 6071.

(15) Kim, Y.-H.; Cho, H.; Heo, J. H.; Kim, T.-S.; Myoung, N.; Lee, C.-L.; Im, S. H.; Lee, T.-W. Multicolored Organic/Inorganic Hybrid Perovskite Light-Emitting Diodes. *Adv. Mater.* **2015**, *27*, 1248−1254.

(16) Lim, K.-G.; Kim, H.-B.; Jeong, J.; Kim, H.; Kim, J. Y.; Lee, T.-W. Boosting the Power Conversion Efficiency of Perovskite Solar Cells Using Self-Organized Polymeric Hole Extraction Layers with High Work Function. *Adv. Mater.* **2014**, *26*, 6461−6466.

(17) Momblona, C.; Malinkiewicz, O.; Roldán-Carmona, C.; Soriano, A.; Gil-Escrig, L.; Bandiello, E.; Scheepers, M.; Edri, E.; Bolink, H. J. Efficient Methylammonium Lead Iodide Perovskite Solar Cells with Active Layers from 300 to 900 nm. *APL Mater.* **2014**, *2*, 081504.

(18) Eperon, G. E.; Stranks, S. D.; Menelaou, C.; Johnston, M. B.; Herz, L. M.; Snaith, H. J. Formamidinium Lead Trihalide: a Broadly Tunable Perovskite for Efficient Planar Heterojunction Solar Cells. *Energy Environ. Sci.* **2014**, *7*, 982−988.

(19) Xing, G.; Mathews, N.; Sun, S.; Sien Lim, S.; Ming Lam, Y.; Grätzel, M.; Mhaisalkar, S.; Chien Sum, T. Long-Range Balanced Electron- and Hole-Transport Lengths in Organic-Inorganic $CH_3NH_3PbI_3$. *Science* **2013**, *342*, 344−347.

(20) Stranks, S. D.; Eperon, G. E.; Grancini, G.; Menelaou, C.; Alcocer, M. J. P.; Leijtens, T.; Herz, L. M.; Petrozza, A.; Snaith, H. J. Electron-Hole Diffusion Lengths Exceeding 1 Micrometer in an Organometal Trihalide Perovskite Absorber. *Science* **2013**, *342*, 341−344.

(21) Gonzalez-Pedro, V.; Juarez-Perez, E. J.; Arsyad, W.-S.; Barea, E. M.; Fabregat-Santiago, F.; Mora-Sero, I.; Bisquert, J. General Working Principles of $CH_3NH_3PbX_3$ Perovskite Solar Cells. *Nano Lett.* **2014**, *14*, 888−893.

(22) Zhao, Y.; Nardes, A. M.; Zhu, K. Solid-State Mesostructured Perovskite $CH_3NH_3PbI_3$ Solar Cells: Charge Transport, Recombination, and Diffusion Length. *J. Phys. Chem. Lett.* **2014**, *5*, 490−494.

(23) Wehrenfennig, C.; Eperon, G. E.; Johnston, M. B.; Snaith, H. J.; Herz, L. M. High Charge Carrier Mobilities and Lifetimes in Organolead Trihalide Perovskites. *Adv. Mater.* **2014**, *26*, 1584−1589.

(24) Wehrenfennig, C.; Liu, M.; Snaith, H. J.; Johnston, M. B.; Herz, L. M. Charge-Carrier Dynamics in Vapour-Deposited Films of the Organolead Halide Perovskite $CH_3NH_3PbI_{3−x}Cl_x$. *Energy Environ. Sci.* **2014**, *7*, 2269−2275.

(25) Savenije, T. J.; Ponseca, C. S., Jr.; Kunneman, L.; Abdellah, M.; Zheng, K.; Tian, Y.; Zhu, Q.; Canton, S. E.; Scheblykin, I. G.; Pullerits, T.; et al. Thermally Activated Exciton Dissociation and Recombination Control the Carrier Dynamics in Organometal Halide Perovskite. *J. Phys. Chem. Lett.* **2014**, *5*, 2189−2194.

(26) Edri, E.; Kirmayer, S.; Henning, A.; Mukhopadhyay, S.; Gartsman, K.; Rosenwaks, Y.; Hodes, G.; Cahen, D. Why Lead Methylammonium Tri-Iodide Perovskite-Based Solar Cells Require a Mesoporous Electron Transporting Scaffold (but Not Necessarily a Hole Conductor). *Nano Lett.* **2014**, *14*, 1000−1004.

(27) Edri, E.; Kirmayer, S.; Mukhopadhyay, S.; Gartsman, K.; Hodes, G.; Cahen, D. Elucidating the Charge Carrier Separation and Working Mechanism of $CH_3NH_3PbI_{3−x}Cl_x$ Perovskite Solar Cells. *Nat. Commun.* **2014**, *5*, 3461.

(28) Akselrod, G. M.; Prins, F.; Poulikakos, L. V.; Lee, E. M. Y.; Weidman, M. C.; Mork, A. J.; Willard, A. P.; Bulović, V.; Tisdale, W. A. Subdiffusive Exciton Transport in Quantum Dot Solids. *Nano Lett.* **2014**, *14*, 3556−3562.

(29) Guo, Z.; Manser, J. S.; Wan, Y.; Kamat, P. V.; Huang, L. Spatial and Temporal Imaging of Long-Range Charge Transport in Perovskite Thin Films by Ultrafast Microscopy. *Nat. Commun.* **2015**, *6*, 7471.

(30) Li, Y.; Yan, W.; Li, Y.; Wang, S.; Wang, W.; Bian, Z.; Xiao, L.; Gong, Q. Direct Observation of Long Electron-Hole Diffusion Distance in $CH_3NH_3PbI_3$ Perovskite Thin Film. *Sci. Rep.* **2015**, *5*, 14485.

(31) Snaith, H. J.; Abate, A.; Ball, J. M.; Eperon, G. E.; Leijtens, T.; Noel, N. K.; Stranks, S. D.; Tse-Wei Wang, J.; Wojciechowski, K.; Zhang, W. Anomalous Hysteresis in Perovskite Solar Cells. *J. Phys. Chem. Lett.* **2014**, *5*, 1511−1515.

(32) Unger, E. L.; Hoke, E. T.; Bailie, C. D.; Nguyen, W. H.; Bowring, A. R.; Heumüller, T.; Christoforo, M. G.; McGehee, M. D. Hysteresis and Transient Behavior in Current-Voltage Measurements of Hybrid-Perovskite Absorber Solar Cells. *Energy Environ. Sci.* **2014**, *7*, 3690−3698.

(33) Baumann, A.; Tvingstedt, K.; Heiber, M. C.; Väth, S.; Momblona, C.; Bolink, H. J.; Dyakonov, V. Persistent Photovoltage in Methylammonium Lead Iodide Perovskite Solar Cells. *APL Mater.* **2014**, *2*, 081501.

(34) Yamada, Y.; Endo, M.; Wakamiya, A.; Kanemitsu, Y. Spontaneous Defect Annihilation in $CH_3NH_3PbI_3$ Thin Films at Room Temperature Revealed by Time-Resolved Photoluminescence Spectroscopy. *J. Phys. Chem. Lett.* **2015**, *6*, 482−486.

(35) Barrows, A. T.; Pearson, A. J.; Kyu Kwak, C.; Dunbar, A. D. F.; Buckley, A. R.; Lidzey, D. G. Efficient Planar Heterojunction Mixed-Halide Perovskite Solar Cells Deposited Via Spray-Deposition. *Energy Environ. Sci.* **2014**, *7*, 2944−2950.

(36) Mei, A.; Li, X.; Liu, L.; Ku, Z.; Liu, T.; Rong, Y.; Xu, M.; Hu, M.; Chen, J.; Yang, Y.; et al. A Hole-Conductor-Free, Fully Printable Mesoscopic Perovskite Solar Cell with High Stability. *Science* **2014**, *345*, 295−298.

(37) Zhao, C.; Chen, B.; Qiao, X.; Luan, L.; Lu, K.; Hu, B. Perovskite Solar Cells: Revealing Underlying Processes Involved in Light Soaking Effects and Hysteresis Phenomena in Perovskite Solar Cells. *Adv. Energy Mater.* **2015**, *5*, 1500279.

(38) Acket, G. A.; Nijman, W.; 't Lam, H. Electron Lifetime and Diffusion Constant in Germanium-Doped Gallium Arsenide. *J. Appl. Phys.* **1974**, *45*, 3033−3040.

(39) Schlipf, J.; Docampo, P.; Schaffer, C. J.; Körstgens, V.; Bießmann, L.; Hanusch, F.; Giesbrecht, N.; Bernstorff, S.; Bein, T.; Müller-Buschbaum, P. A Closer Look into Two-Step Perovskite Conversion with X-ray Scattering. *J. Phys. Chem. Lett.* **2015**, *6*, 1265−1269.

(40) Hoke, E. T.; Slotcavage, D. J.; Dohner, E. R.; Bowring, A. R.; Karunadasa, H. I.; McGehee, M. D. Reversible Photo-Induced Trap Formation in Mixed-Halide Hybrid Perovskites for Photovoltaics. *Chem. Sci.* **2015**, *6*, 613−617.

(41) Shi, D.; Adinolfi, V.; Comin, R.; Yuan, M.; Alarousu, E.; Buin, A.; Chen, Y.; Hoogland, S.; Rothenberger, A.; Katsiev, K.; et al. Low Trap-State Density and Long Carrier Diffusion in Organolead Trihalide Perovskite Single Crystals. *Science* **2015**, *347*, 519−522.